JGR Planets

RESEARCH ARTICLE

10.1029/2024JE008353

High Pressure Melting Curve of Fe-Si: Implication for the Thermal Properties in Mercury's Core

Innocent C. Ezenwa[1,2], **Yingwei Fei**[1], **Rostislav Hrubiak**[2], **and Curtis Kenney-Benson**[2]

[1]Carnegie Institution for Science, Washington, DC, USA, [2]HPCAT, Advanced Photon Source, Argonne National Laboratory, Chicago, IL, USA

Key Points:

- Determination of the high pressure melting curve of Fe-Si using in situ and ex situ intermetallic fast diffusion technique
- Provided constraint on the melting temperature profile of Mercury's core
- Provided a constraint on the thermal conductivity and heat flux at Mercury's core-mantle and inner-core (assumed at 21 GPa) boundaries

Supporting Information:

Supporting Information may be found in the online version of this article.

Correspondence to:

I. C. Ezenwa,
iezenwa@anl.gov

Citation:

Ezenwa, I. C., Fei, Y., Hrubiak, R., & Kenney-Benson, C. (2024). High pressure melting curve of Fe-Si: Implication for the thermal properties in Mercury's core. *Journal of Geophysical Research: Planets*, *129*, e2024JE008353. https://doi.org/10.1029/2024JE008353

Received 29 FEB 2024
Accepted 28 OCT 2024

Author Contributions:

Conceptualization: Innocent C. Ezenwa, Yingwei Fei
Formal analysis: Innocent C. Ezenwa
Funding acquisition: Yingwei Fei
Investigation: Innocent C. Ezenwa
Methodology: Innocent C. Ezenwa, Curtis Kenney-Benson
Resources: Yingwei Fei, Rostislav Hrubiak, Curtis Kenney-Benson
Supervision: Yingwei Fei
Writing – original draft: Innocent C. Ezenwa
Writing – review & editing: Innocent C. Ezenwa, Yingwei Fei, Rostislav Hrubiak

Abstract The motion of liquid iron (Fe) alloy materials in the outer core drives the dynamo, which generates Mercury's magnetic field. The assessment of core models requires laboratory measurements of the melting temperature of Fe alloys at high pressure. Here, we experimentally determined the melting curve of Fe9wt%Si and Fe17wt%Si up to 17 GPa using in situ and ex situ measurements of intermetallic fast diffusion that serves as the melting criterion in a large-volume press. Our determined melting slopes are comparable with previous studies up to about 17 GPa. However, when extrapolated, our melting slopes significantly deviate from previous studies at higher pressures. For Mercury's core with a model composition of Fe9wt%Si, the melting temperature-depth profile determined in our study is lower by ∼150–250 K when compared with theoretical calculations. Using the new melting curve of Fe9wt%Si and the electrical resistivity values from a previous study of Fe8.5wt%Si, we estimate that the electronic thermal conductivity of liquid Fe9wt%Si is 30 $Wm^{-1}K^{-1}$ at the Mercury's *CMB* pressure of 5 GPa and 37 $Wm^{-1}K^{-1}$ at an assumed *ICB* of 21 GPa, corresponding to heat flux values of 23 mWm^{-2} and 32 mWm^{-2}, respectively. These values provide new constraints on the core models.

Plain Language Summary The thermal structure and evolution of the cores of the rocky planets and their satellites are constrained by the thermal properties of Fe plus light elements determined under extreme conditions. Here, we closely determine the melting temperature of iron (Fe)-silicon (Si) systems by in situ and ex situ characterization of the inter-metallic diffusive reaction of Fe-Si and tungsten (W) at the melting transition. We measured the melting temperatures of Fe9wt%Si and Fe17wt%Si at various fixed pressures up to 17 GPa. Our data sets provide a tighter constraint on the melting curve of Fe-Si measured in the large-volume press. Using our determined melting curve of Fe9wt%Si and the electrical resistivity values from a previous study of Fe8.5wt%Si at similar pressure conditions, we estimated the thermal conductivity and the heat flux at the core-mantle boundary and inner core boundary (assumed at 21 GPa) of Mercury.

1. Introduction

The chemical compositions and physical properties of the planetary cores are generally inferred indirectly from seismology, geomagnetism, geodesy, and mineral physics, combined with cosmochemical constraints. Light alloying elements (such as Si, S, O, H etc.) affect the crystallization of the dominantly metallic iron (Fe) core as well as the convective style in its liquid outer part (Davies & Pommier, 2018; Hemingway & Driscoll, 2021). A liquid outer core not only exists in the Earth but also in other terrestrial planets and satellites such as Mercury, Mars, Ganymede, and the Moon (e.g., Fei & Bertka, 2005; Margot et al., 2007; Weber et al., 2011). Convective flow in the liquid core drives the dynamo, which generates the magnetic field. The understanding of this process requires knowledge of the physical properties of the liquid core, which depends on the thermal state of the core. Therefore, the assessment of the melting temperature of Fe alloys at high pressure is essential in the modeling of core dynamics. Recently, a new magnetic model reproduced the thermal and magnetic evolution found in the geological record when a relatively low value of the melting temperature of Fe alloy materials at Earth's core pressure and temperature conditions was adopted (Driscoll & Davies, 2023). Thus, it is important to re-assess the melting curve of Fe alloys at readily accessible pressure and temperature conditions appropriate to Mercury. The experimental measurements can be directly applied to Mercury's core without extrapolation, which may shed light on the cores of the Earth and other planets that require measurements at much high pressure and temperature conditions.

Mercury is the most unusual rocky planet in our solar system because of its large metallic core. Its proximity to the Sun poses a hindrance to observational studies. There have only been two missions to Mercury, with a third one currently on its way. Although we do not know its interior structure well enough when compared with other terrestrial planets, Mercury's density, rotational speed, and the presence of a global magnetic field suggest that it has a very large Fe-alloy core with a partially molten outer core (Anderson et al., 1987). Its core size was constrained to about 2,020 km by measurements of the moment of inertia and average density (e.g., Hauck et al., 2013; Rivoldini & Van Hoolst, 2013). Based on the surface abundance of sulfur (S) and Fe, the oxygen fugacity of Mercury's interior was constrained between −2.6 and −7.3 log units below the Fe-FeO buffer (e.g., McCubbin et al., 2017; Zolotov et al., 2013). Because of this highly reducing condition, Sulfur (S) preferentially partitions into the silicate mantle while silicon (Si) partitions into the core during core-mantle segregation (e.g., Gessmann et al., 2001). At a pressure of 2.5 GPa, temperature of 2023 K and oxygen fugacity of −6.67 relative to Fe-FeO buffer condition, Gessmann et al. (2001) demonstrated that about 8.08 wt% Si dissolved into liquid Fe (containing Si of about 6.53 wt% and up to 2.6 wt% S) when it was equilibrated with silicate melt in the presence of magnesiowüstite and olivine. Studies have suggested that about 10.5 wt%Si would be a plausible value of Si content in Mercury's core (Steinbrügge et al., 2021; Terasaki et al., 2019). Interestingly, element partitioning experiments indicated that Si would partition equally between liquid and solid Fe in the pressure range applicable to Mercury's core (Tao & Fei, 2021) with a core-mantle boundary (CMB) pressure of approximately 5–7 GPa (e.g., Hauck et al., 2013). Assuming an inner core radius of about two-thirds the size of its entire core, Ezenwa and Fei (2023) estimated an upper bound temperature at Mercury's inner core boundary (ICB) to be 2180 K at 21 GPa based on the melting temperature of Fe. Since Mercury's core is largely alloyed with Si, the knowledge of the melting curve of the Fe-Si system at high pressure and temperature would aid in the modeling of its core thermal evolution as well as its magnetic field generation, sustainability, and morphology.

Although the melting curve and phase relation in Fe-Si systems have been studied at pressure conditions in the laser-heated diamond-anvil cell with a focus on the Earth's core pressure (e.g., Asanuma et al., 2008; Fischer et al., 2012, 2013; Ozawa et al., 2016), there are only few studies carried out in the pressure range applicable to Mercury's core. Using a large-volume press, Yang and Secco (1999) studied the melting curve of Fe17%Si up to 5.5 GPa, while Kuwayama and Hirose (2004) determined the phase relation in the Fe-FeSi system at 21 GPa. Edmund et al. (2022) also reported the Fe-FeSi phase relation at 25 GPa using the diamond anvil technique. In this study, we determined the high-pressure melting curve of Fe9wt%Si and Fe17wt%Si up to 17 GPa using in situ and ex situ intermetallic fast diffusion as the melting criterion in a large-volume press.

Because the thermal conductivity at the melting boundary depends on the melting temperature, it is critical to evaluate this quantity using the melting temperature data. In general, the electronic thermal conductivity (k_e) of metals and metallic alloys, which dominates their total thermal conductivity (k_c), can be related to their electrical resistivity (ρ) via Wiedemann-Franz's law as follows: $k_e = \frac{L_o T}{\rho}$, where L_o is the Lorenz number and T is the melting temperature. Using this approach, several studies have determined the k_e of metals and metallic alloys at various pressure and temperature conditions by measuring the temperature-dependent electrical resistivity (e.g., Ezenwa & Yoshino, 2020, 2021; Ohta et al., 2016; Silber et al., 2019; Yin et al., 2022; Zhang et al., 2020) across the melting transition. The melting temperatures were determined in these studies by monitoring the change in resistivity across melting. For metals with a high magnetic moment such as Fe, the change in resistivity on melting is quite small at 1 atm (e.g., Chu & Chi, 1981). Although with increasing pressure, the jump in resistivity of Fe would somewhat become larger (Ezenwa & Secco, 2019; Ezenwa & Yoshino, 2021), increasing Si content in Fe significantly decreases the jump in resistivity (Berrada et al., 2021; Silber et al., 2019). As a result, it is challenging to determine the melting temperature of Fe alloys with high impurities via resistivity measurements. Our determined melting temperature by intermetallic fast diffusion technique will provide tighter constraint on the k_e in these alloys along their pressure-dependent melting boundary. Using the determined quantity along with other parameters estimated from previous studies, the heat flux at the CMB and ICB of Mercury can be calculated.

2. Experimental Details

2.1. Ex-Situ Intermetallic Fast Diffusion: Multianvil Cell Assembly

Similar to our recent investigation of the melting curve of Fe using inter-metallic fast diffusion of tungsten (W) in pure Fe (Ezenwa & Fei, 2023), the starting samples in this study were a W disk and Fe-Si powder mixture (Fe9wt%Si or Fe17wt%Si) contained in a cylindrical alumina tube. The Fe-Si starting materials were sourced

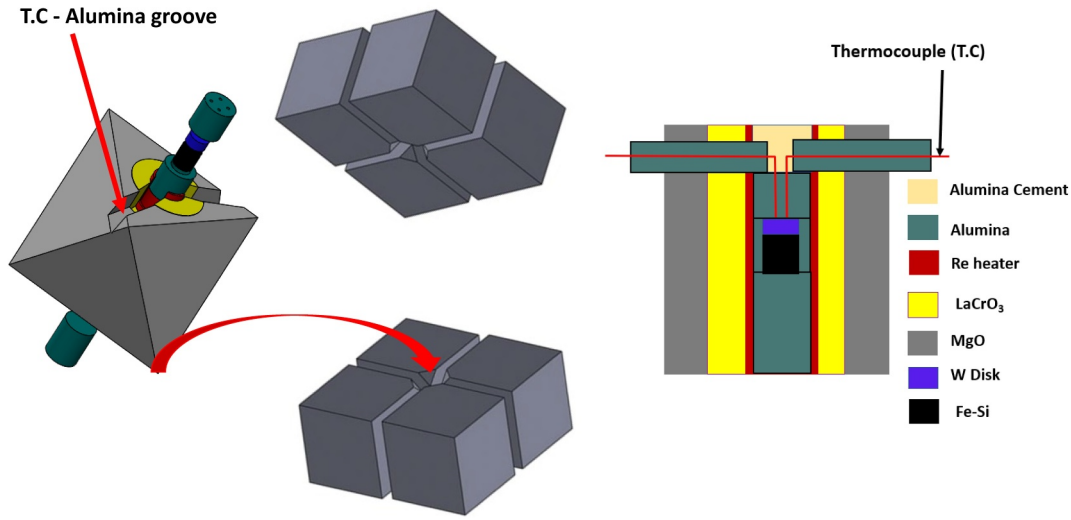

Figure 1. 3D (SolidWorks) and 2D diagram of the 8/3 multi-anvil assembly.

from Goodfellow. The disk was made from a 0.2 mm foil that was purchased from GoodFellow (purity 99.9%). All ceramic parts were baked in an oven at 1273 K for 3 hr. The assembled cell was stored in an oven at 1 atm and 393 K before loading it into the multi-anvil press. The schematic diagram of the cell assembly is shown in Figure 1. The W disk has a diameter and thickness of 0.8 and 0.2 mm, respectively. The disk diameter matched the diameter of the alumina sleeve container and was placed at the base of the alumina sleeve. The powder was packed to the brim of the alumina sleeve with a height of 1 mm. The thermocouple (TC) lead wires were made of W5%Re and W26%Re alloys (Type C) and were placed in a four-hole cylindrical alumina, forming a crossed-like junction at the base of the four-hole alumina. The TC junction is in direct contact with the W disk. The pressure was calibrated using fixed phase transition points (Bertka & Fei, 1997; Hirose & Fei, 2002) and the effect of pressure on the thermocouple readings was not corrected. The estimated error in pressure is about ±1 GPa. The heat source was provided by passing a high current through a cylindrical rhenium (Re) heater surrounding the sample container while a $LaCrO_3$ sleeve placed next to the heater served as a thermal insulator. The pressure and temperature were electronically controlled through an in-house developed computer program.

Experiments were performed at pressures between 8 and 17 GPa and the quenched samples were examined ex situ with a Zeiss Auriga field emission scanning electron microscope (SEM). We prepared consistent cell assembly parts to minimize systematic errors and adopted the same experimental procedure for all the runs. The samples were isothermally compressed at 297 K and then heated to the target temperature at a rate of about 100 K per minute. The sample was kept at the target temperature for 2 min before quenching by cutting off the electrical current. The sample was subsequently decompressed to ambient pressure. The post-mortem cell assembly was mounted in epoxy resin and polished along the long axis of the heater to expose the W and Fe-Si sample for chemical analyses. To characterize the W/Fe-Si interaction and examine the change in the diffusivity at the melting transition, we obtained secondary electron image (SEI) and electron probe microanalysis (EPMA) data on the recovered sample. We used an accelerating voltage of 15 kV, a probe current of 30 nA and a spot size of approximately 100 nm for all the analyses. At each fixed pressure, several runs with different target temperatures were performed to determine the chemical change at the interface of W and Fe-Si alloy as a function of temperature. The W interaction with Fe-Si alloy provides a clear indication for the solid to liquid transition. For each fixed pressure, we placed the melting temperature of the sample between the highest temperature on the solid side and the lowest temperature on the liquid phase. The procedure was repeated at various fixed pressure points to determine the corresponding melting temperatures up to 17 GPa.

2.2. In-Situ Intermetallic Fast Diffusion: Paris Edinburgh (PE) Cell Assembly

The in situ experiments were conducted at 16-BMB beamline of the High Pressure Collaborative Access Team (HPCAT) at the Advanced Photon Source. A Paris Edinburgh (PE) press cell assembly (see, Kono et al., 2014) with a cylindrical sample container made of boron nitride (BN) was adopted (Figure 2). Before the experiments,

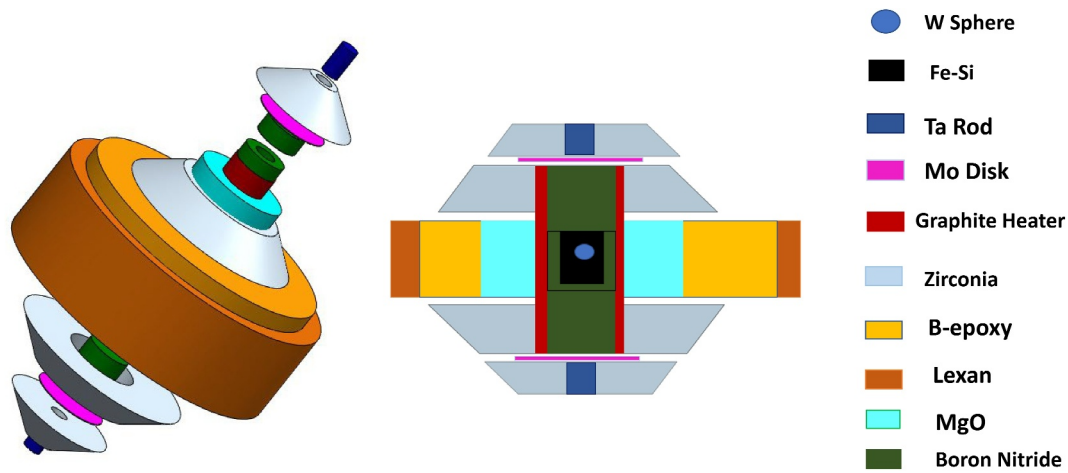

Figure 2. 3D (SolidWorks) and 2D schematic diagram of PE cell.

x-ray photon energy and 2-theta calibration of the energy dispersive diffraction setup were performed. Energy calibration of the energy-dispersive detector (ultra-high purity germanium) was performed using gamma rays from ^{109}Cd (88.04 keV) and ^{57}Co (122.10 keV). The 2-theta calibration was performed using a gold wire as the d-spacings standard. The sample diameter and height were 1 and 1.5 mm, respectively. For each run, either Fe9wt% Si or Fe17wt%Si was compacted inside the container and a W sphere of diameter ~150–200 microns was placed in the middle of the sample container using a micro-manipulator.

Energy dispersive x-ray diffraction (EDXD) was performed on the sample and the MgO pressure standard at a fixed 2-theta angle under various pressure and temperature conditions to determine the crystalline state of the sample and to estimate the sample pressure using the equation of state of MgO (Kono et al., 2010). The error in pressure in the adopted cell assembly is 0.2 GPa within the pressure range of our investigation. Temperature was determined based on calibrated power-temperature relationship at various fixed loads established in a separate experiment using an identical cell assembly. Using this relation, the melting temperature of Fe determined by Kono et al. (2015) was consistent with the measurements by Terasaki et al. (2002) and Rutter et al. (2002). Diffusion of W with Fe-Si was observed through X-ray radiography using a high-speed camera (Photron SA3). The pixel size of the high-speed camera was calibrated (0.9745 microns/pixel) using a precisely measured tungsten carbide (WC) sphere of 497 μm as a scale reference. The samples were heated at a rate of about 100 K per minute up to a temperature of about 300 K below the anticipated melting temperature and were monitored with a low speed (40–50 fps) radiography camera. Above this temperature, the radiographic image of the sample was acquired using a high-speed camera. For this, we adopted a frame rate of 700 fps with 2 ms exposure time. At high temperature close to melting, the expected solid-solid diffusion of W into Fe-Si forming a layer of W-Fe-Si was evidenced as a dark gray-scale image at the interface between W and Fe-Si (Figure 3). On melting, the W-Fe-Si layer was observed reacting with the remaining pure Fe-Si sample, which subsequently led to the disappearance of the sphere. Due to the density contrast between W and Fe-Si, the W sphere moved a distance of about 50–100 microns while rapidly dissolving into the molten Fe-Si. The dissolution lasted for about 8 s. The average of the sample temperatures recorded at the onset and end of reaction was taken as the melting temperature of Fe-Si at the fixed pressure. The attainment of melting temperature was also supported by the appearance of diffuse X-ray diffraction scattering of the sample (Figure 3). In situ runs were performed at determined pressures of 2.4 and 4.6 GPa for Fe9wt%Si and 2 and 5 GPa for Fe17wt%Si. Due to the infinitesimal size of the W sphere, there was no evidence of W peak in the XRD pattern collected from the quenched sample. The W content could also be difficult to chemically detect and quantify in the Fe-Si matrix.

3. Results and Discussions

3.1. Detection of Melting Transition in Fe-Si by Intermetallic Diffusion

Before melting, the SEI image and the EPMA data (Figure 4 and Figure S1 in Supporting Information S1) show a formation of two (gray colored) regions whose textures appear interdiffusion like, labeled region I and II. Region I

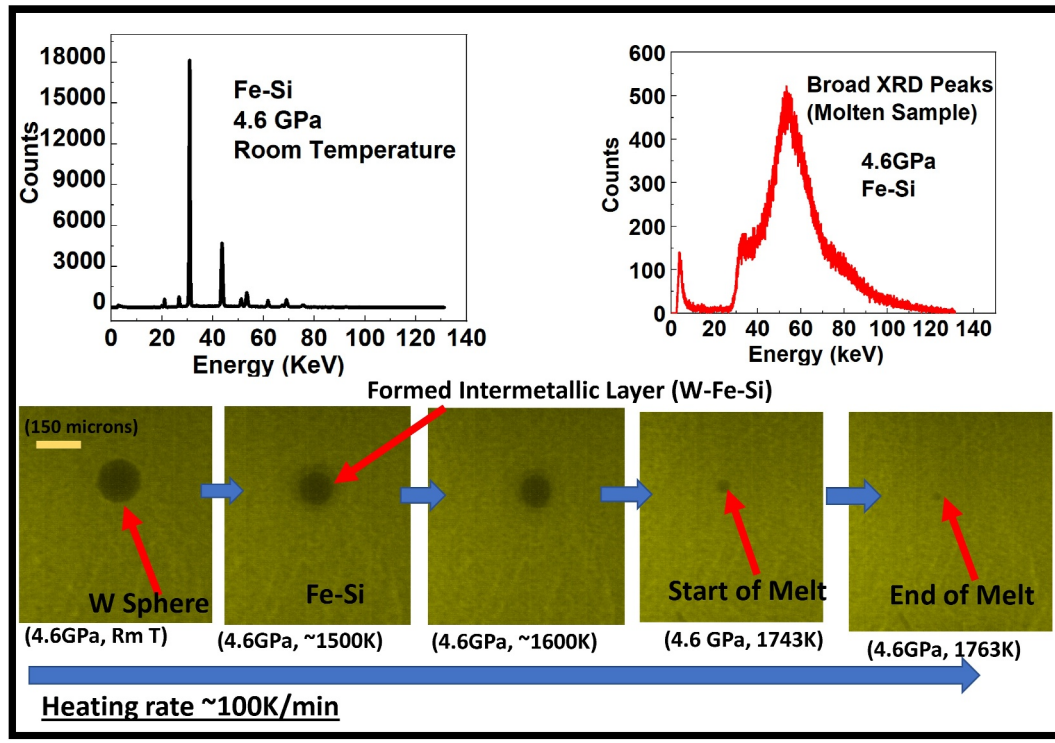

Figure 3. Radiographic image of W sphere recorded with a speed Camera during heating up to melting and the EDXD pattern of the sample in its solid and molten states. The temperatures at the "start of melt" and "end of melt" were recorded as the solid and liquid state data respectively.

could correspond to Fe-Si diffused into W, while region II corresponds to W diffused into Fe-Si. Both of these regions could have different diffusion rates at a given pressure and temperature condition which could give rise to the differences in the observed area of coverage. On melting, a transition from long-range to short-range order on melting (Lennard-Jones & Devonshire, 1939) leads to an increase in the degree of freedom of atomic motion, which in turn causes an abrupt increase in the diffusivity of W into Fe-Si, as evidenced in the wide spread of W in the Fe-Si matrix with an average content of 10.5 wt% (Figure 4). Also, dendritic texture that could characterize melting is evidenced in the Fe-Si melt of the recovered samples. The complete data set of all the runs (ex situ and in situ) obtained in this study is shown in Figure 5 and Table S3 of Supporting Information S1. Using these data sets, we constructed the melting curves of Fe9wt%Si and Fe17wt%Si up to our maximum investigated pressure of 17 GPa.

3.2. Melting Curve of Fe-Si

Although Fe9wt%Si and Fe17wt%Si alloys represent compositions in a binary system with solidus and liquidus boundaries, their melting phase relations at ambient pressure (Meco & Napolitano, 2005; Schurmann & Hensgen, 1980), 5.5 GPa (Yang & Secco, 1999), and 21 GPa (Edmound et al., 2022; Kuwayama & Hirose, 2004) suggest that the solidus and liquidus temperature are very close in value with a narrow loop of approximately 10 K. Hence, the melting temperatures at different pressure points determined in this study (Figure 6) represent the average values of the solidus and the liquidus temperature. The data sets are available in Tables S1 and S2 of Supporting Information S1. As expected, the melting temperature increases with pressure for both compositions but decreases with increasing Si content. The change in the dT/dP of the melting curve reflects the change in the volume difference between solid and liquid as a function of pressure due to the difference in their compressibility. The melting curve of Fe9wt%Si and Fe17wt%Si were fitted with Simon-Glatzel equation; $T_m = T_o\left(\frac{P-P_o}{a}+1\right)^b$ where T_o is the melting temperature at a reference pressure P_o. T_m is the melting temperature at any given pressure P. "a" and "b" are the fitted parameters. For Fe9wt%Si, the fitted curve yielded $a = 17.59 \pm 10.01$ GPa and $b = 0.25 \pm 0.11$. For 17wt%Si, the fitted curve yielded $a = 10 \pm 6.13$ GPa and $b = 0.23 \pm 0.09$. In comparison

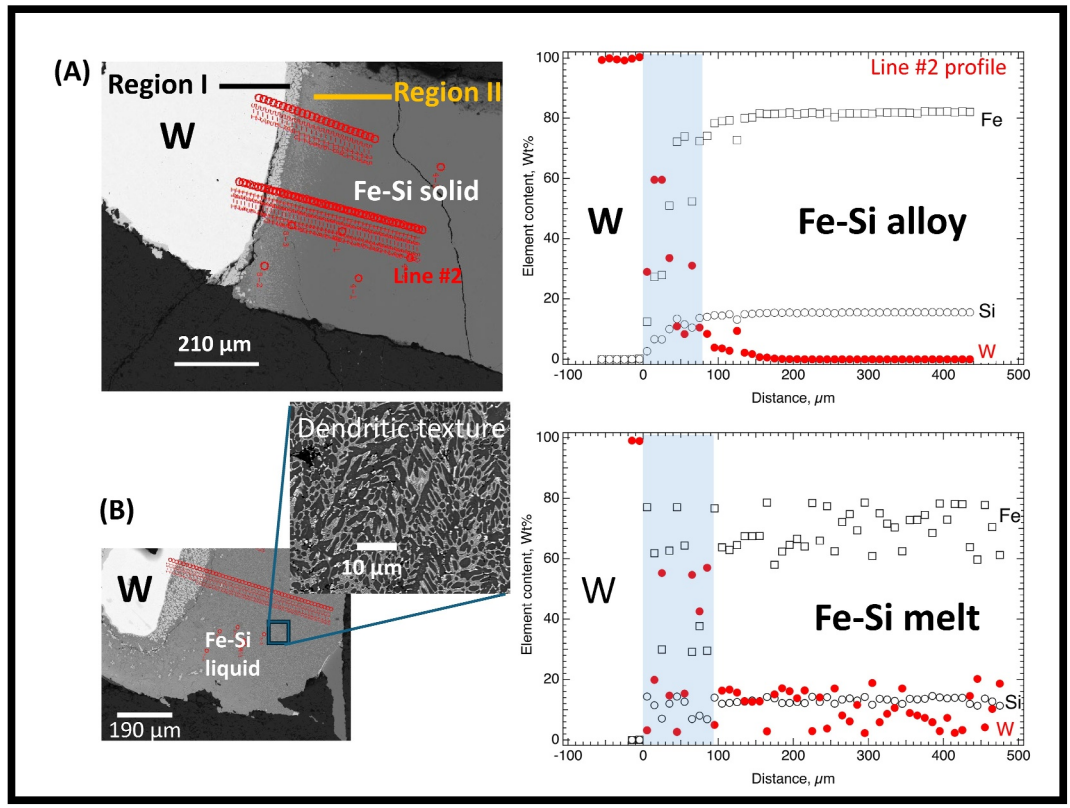

Figure 4. W, Fe, and Si analysis across the W - Fe17wt%Si interface before and after melting transition. (a) W, Fe, and Si profiles measured on the recovered sample at 10 GPa and 1753 K. The line profile shows only W on the W side and limited W diffusion into the Fe-Si alloy. The shaded areas indicate the intermetallic boundary layer. No W was detected in the interior of the alloy, indicating the solid state of the alloy. (b) W, Fe, and Si profiles measured on the recovered sample at 10 GPa and 1783 K. The sample was molten based on the W distribution across the sample supported by the dendritic quench texture. The measured elemental variation in the Fe-Si melt reflects the fine dendritic texture with an average W content of 10.5 wt%.

with previous experimental melting curve data for Fe17wt%Si measured up to 5.5 GPa (Yang & Secco, 1999), our determined melting curve agrees within uncertainty. The melting temperatures of Fe9wt%Si and Fe17wt%Si obtained from the Fe-Si phase diagram study by Kuwayama and Hirose (2004) at 21 GPa is about 300 K higher than that determined in this study. The estimated Fe-Si solidus line reported by Edmund et al. (2022) is comparable to our melting curve up to about 18 GPa. Above 18 GPa, the trend of our melting curve is lower than theirs (Figure 6). The melting slopes reported by Fischer et al. (2012, 2013) are significantly steeper and would lead to a large difference in melting temperature at high pressure (Figure 6).

The structure of the solid phase preceding melting has influence on the slope of the melting curve slope of Fe (Sanloup et al., 2000). The solid solution of Fe-Si undergoes a structural transformation sequence similar to pure Fe with increasing pressure and temperature. It is well known that body-centered cubic *(bcc)* Fe would transform to a hexagonal closed packed *(hcp)* structure at ~10–18 GPa and 300 K (Jamieson & Lawson, 1962; Mao et al., 1967; Yamazaki et al., 2012). At high temperatures, both *bcc* and hcp phases transform to face-centered cubic *(fcc)* structures (Bundy, 1965) with an fcc-hcp-melting triple point near 100 GPa. For the Fe-Si system, an experimental study by Zhang and Guyot (1999) demonstrated that at ~ 6–9 GPa, the onset of the transformation of *bcc-fcc* in Fe9wt%Si occurred at temperatures about 300 K higher than that in pure Fe, indicating that Si is a *bcc* stabilizer. At a pressure of 16 GPa, the experimental investigation by Lin et al. (2002) showed that *bcc* + *hcp* would be stabilized in Fe9wt%Si up to 1000 K. Above this temperature, *bcc* + *fcc* was stable up to their maximum investigated temperature of 1500 K. Data from Lin et al. (2002) are consistent with the study of Fischer et al. (2012, 2013) that reported phase relations of Fe9wt%Si alongside other compositions (Fe, Fe16wt%, and FeSi). In Fe16wt%Si, which is very close to our studied composition (Fe17wt%Si), it has been reported that the bcc like structure of DO_3 phase is stable within the pressure range of our investigation. In both Fe9wt%Si and

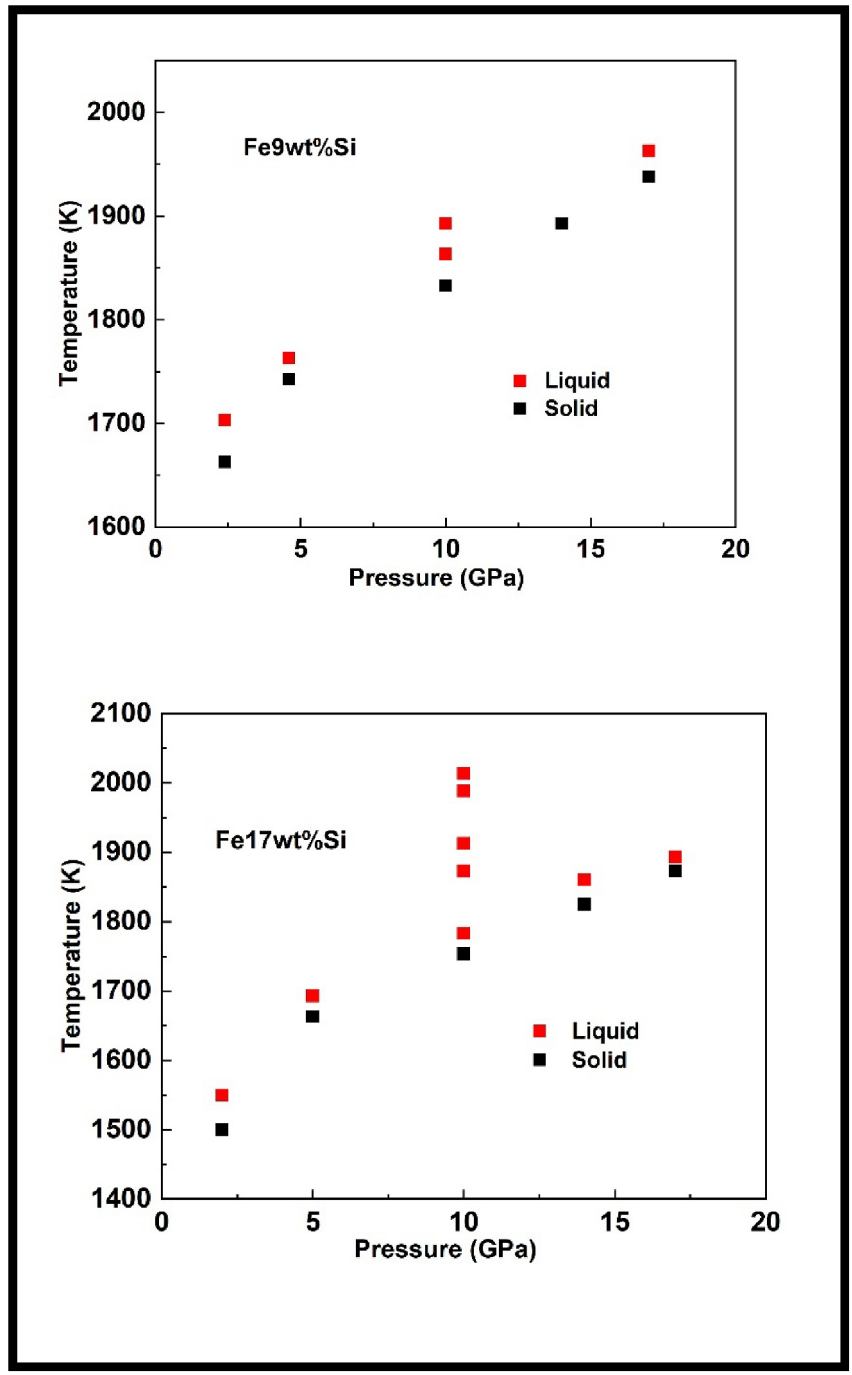

Figure 5. Data set of all the experiments performed at different fixed pressures for Fe9wt%Si and Fe17wt%Si.

Fe16wt%Si, there is no reported phase change in the liquidus phase, which is consistent with our data set, given that there is no change in slope in our determined melting curve. Although all these studies have attempted to understand phase relations in Fe-Si systems, we note that the pressure-dependent phase stability of Fe-Si systems is still not well known at high pressure (e.g., Edmund et al., 2022).

3.3. Thermal Properties in Mercury's Core

Observational studies have provided some constraints in Mercury's thermal evolution (e.g., Marchi et al., 2013; Margot et al., 2007). Measurements taken by NASA's Mercury Surface, Space Environment, Geochemistry, and

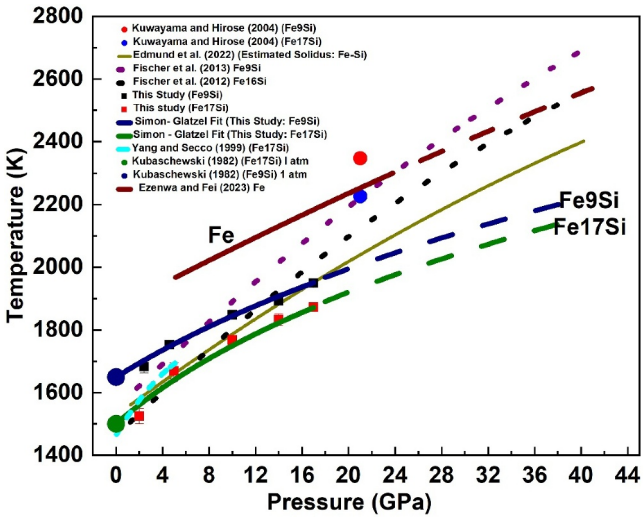

Figure 6. Melting curve of pure Fe determined in our previous study plotted with the melting curve of Fe9wt%Si and Fe17wt%Si as determined in this study and compared with previous studies. The curves were fitted with the Simon-Glatzel equation (see text). The 1 atm data were taken from Kubaschewski (1982).

Ranging (MESSENGER) spacecraft indicate that Mercury's magnetic field is actively generated by a dynamo action in its liquid core (Anderson et al., 2012). The deep core dynamo scenario is supported by modeling works that suggest (e.g., Grott et al., 2011; Hauck et al., 2004; Tosi et al., 2013) that the CMB heat flux became sub-adiabatic in the first billion years after its core formation. Knibbe and van Westrenen (2018) studied the thermal and magnetic field evolution with an Fe-Si core and found matches of Mercury's present-day partially molten state, its magnetic field strength and the observed ancient crustal magnetization. The computed temperature profiles in their core thermal evolution model were based on thermodynamic modeling, mainly utilizing available physical properties of Fe alloys as well as mantle materials properties. Although the assumptions used in determining the temperature profiles prevent unambiguous determination of the planetary internal structure (e.g., Khan et al., 2018), the thermal structure of the core requires constraints on core temperature (e.g., Pommier et al., 2022). The outer core is supposed to be compositionally homogenous and would follow an adiabatic temperature profile if thermal convection is vigorous (e.g., Davies, 2015) or if chemical convection dominates (Loper, 1978). Studies have suggested that about 10.5wt%Si would be a plausible value of Si content in Mercury's core (Steinbrügge et al., 2021; Terasaki et al., 2019). This Si content is close in value to the 9wt%Si sample in our study. Hence, our data set can be directly applied to Mercury's core.

Under hydrostatic core equilibrium conditions, the variation in pressure with radius can be related as $P_{(r)} = \int_r^R \rho_r g_r dr$ (e.g., Hauck et al., 2013). Where R is the entire core radius, ρ_r and g_r are the density and gravity variation with radius respectively. The pressure at the CMB and its radius are estimated to be around 5–7 GPa and ~2,020 km (Hauck et al., 2013; Knibbe & van Westrenen, 2018). With an assumed ICB radius of 1,346 km, the corresponding pressure is estimated to be 21 GPa (Ezenwa & Fei, 2023). With increasing Si content in Fe, liquid Fe-Si appears to have a negligible change in density in the range of Fe (8–40) wt%Si (Tateyama et al., 2011). Similarly, with increasing pressure, the density of liquid Fe17wt%Si only varied by approximately 80 kg/m^3 from 3 GPa up to the maximum investigated pressure of 12 GPa by Yu and Secco (2008). This is consistent with experimental studies that demonstrated that Si does not significantly modify liquid Fe local structure which results in minimal influence in all associated physical properties such as bulk modulus, density, and seismic velocity (Sanloup et al., 2002; Terasaki et al., 2019). Therefore, we accounted for Mercury's density variation with its core radius by taking its value to be 7,070 kg/m^3 at the CMB based on the experimental measurement of Fe9.3wt%Si at 4 GPa and 1923 K (Tateyama et al., 2011). We then varied it linearly with depth up to a value of 7,150 kg/m^3 at ICB. The g_r was taken to be 4 m/s^2 as adopted by many studies (e.g., Rivoldini & Van Hoolst, 2013). Assuming the melting curve of Fe-Si to be the core temperature profile, we interpolated the pressure-depth profile and subsequently derived the melting temperature-depth relationship using the melting temperature versus pressure determined in our study. For Fe9wt%Si, in comparison with the theoretical Fe-Si melting temperature-depth profile, the established melting temperature-depth profile in this study deviates by about 150–250 K (Figure 7). This deviation would be greater if Mercury's core composition contains higher Si content.

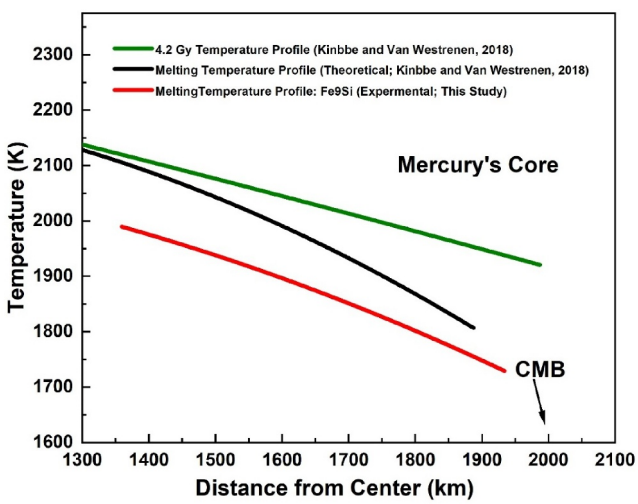

Figure 7. The melting temperature versus distance from Mercury's core center established in this study and compared with the theoretical model from Knibbe and van Westrenen (2018).

The core temperature and thermal conductivity are essential parameters in calculating the adiabatic core heat flux (Q), as described below.

$$Q = k_c \left[\frac{\alpha g T}{C_p}\right]$$

where α is the thermal expansion coefficient, g is the gravitational acceleration, and C_p is the heat capacity at constant pressure. Table 1 shows the

Table 1
Tabulated Parameter Values Used in Calculating the Electronic Thermal Conductivity and Heat Flux at Mercury's CMB and at Assumed ICB Boundaries

Parameters	Values	
	CMB	ICB
Electronic conductivity (k_c)	30 $Wm^{-1}K^{-1}$	37 $Wm^{-1}K^{-1}$
Thermal expansion (α)	8.9×10^{-5} K^{-1}	8.9×10^{-5} K^{-1}
Heat capacity (C_p)	850 J $kg^{-1}K^{-1}$	850 J $kg^{-1}K^{-1}$
Gravity (g)	4 m/s^2	4 m/s^2
Temperature (T)	1754 K	1,996 K
Heat Flux (Q)	23 mWm^{-2}	32 mWm^{-2}

Note. T were determined in this study. k_c and Q were calculated in this study. α was taking from Secco (2017); α, C_p, and g were taking from Rivoldini and Van Hoolst (2013).

values used in this study. From the work of Berrada et al. (2021), the electrical resistivity of Fe8.5wt%Si was determined to be 140 and 127 μΩ.cm at 5 and 20 GPa, respectively. For an assumed Fe9wt%Si core composition, using our melting data (Fe9wt%Si) and these resistivity values, we determine via Wiedemann-Franz's law that the electronic thermal conductivity of liquid Fe9wt%Si is 30 $Wm^{-1}K^{-1}$ at the Mercury's CMB pressure of 5 GPa and 37 $Wm^{-1}K^{-1}$ at an assumed ICB pressure of 21 GPa, corresponding to heat flux values of 23 mWm^{-2} at CMB and 32 mWm^{-2} at ICB. These values are within the range of the estimated Mercurian adiabatic heat flux by previous studies (See Berrada et al., 2021 and ref in) and would provide further constraints on Mercury's core evolution models.

4. Conclusions

The melting curves of Fe9wt%Si and Fe17wt%Si were experimentally determined up to 17 GPa using in situ and ex situ intermetallic fast diffusion as the melting criterion in a large-volume press. In comparison with previous melting curves, our data sets are generally consistent with previous studies at a relatively lower pressure of about 10 GPa. Above this pressure, our determined melting curve deviates up to about 600 K at 40 GPa. In comparison with the theoretical computed melting temperature of Fe-Si at Mercury's core, the determined melting temperature-depth profile in this study for Fe9wt%Si is lower by ~150–250 K. The estimated electronic thermal conductivity of liquid Fe9wt%Si is 30 $Wm^{-1}K^{-1}$ at the Mercury's CMB (~5 GPa) and 37 $Wm^{-1}K^{-1}$ at the ICB (~21 GPa). The corresponding heat flux values are 23 mWm^{-2} and 32 mWm^{-2} respectively, providing new Mercury's core evolution model parameters.

Data Availability Statement

The compiled experimental data and the raw EPMA data are available in the Open Science Framework OSF (Ezenwa et al., 2024).

Acknowledgments
We thank Jing Yang and Emma Bullock for technical assistance, and Joe Lai and Javier Rojas for developing the press control system. We sincerely thank the reviewers for their comments and Emma Bullock for additional chemical analysis during the review process. This research is partially supported by NASA Grant (80NSSC20K0337) and NSF Grant (EAR-2022492) to YF. HPCAT operations are supported by DOE-NNSA's Office of Sciences. The Advanced Photon Source is a U.S. Department of Energy (DOE) Office of Experimental Science User Facility operated by the DOE Office of Science by Argonne National Laboratory under Contract No. DE-AC02-06CH11357.

References

Anderson, B. J., Johnson, C. L., Korth, H., Winslow, R. M., Borovsky, J. E., Purucker, M. E., et al. (2012). Low-degree structure in Mercury's planetary magnetic field. *Journal of Geophysical Research*, *117*(E12). https://doi.org/10.1029/2012je004159

Anderson, J. D., Colombo, G., Esposito, P. B., Lau, E. L., & Trager, G. B. (1987). The mass, gravity field, and ephemeris of Mercury. *Icarus*, *71*(3), 337–349. https://doi.org/10.1016/0019-1035(87)90033-9

Asanuma, H., Ohtani, E., Sakai, T., Terasaki, H., Kamada, S., Hirao, N., et al. (2008). Phase relations of Fe-Si alloy up to core conditions: Implications for the Earth inner core. *Geophysical Research Letters*, *35*(12). https://doi.org/10.1029/2008gl033863

Berrada, M., Secco, R. A., & Yong, W. (2021). Adiabatic heat flow in Mercury's core from electrical resistivity measurements of liquid Fe-8.5 wt% Si to 24 GPa. *Earth and Planetary Science Letters*, *568*, 117053. https://doi.org/10.1016/j.epsl.2021.117053

Bertka, C. M., & Fei, Y. (1997). Mineralogy of the Martian interior up to core-mantle boundary pressures. *Journal of Geophysical Research*, *102*(B3), 5251–5264. https://doi.org/10.1029/96jb03270

Bundy, F. P. (1965). Pressure—Temperature phase diagram of iron to 200 kbar, 900 C. *Journal of Applied Physics*, *36*(2), 616–620. https://doi.org/10.1063/1.1714038

Chu, T. K., & Chi, T. C. (1981). Properties of selected ferrous alloying elements.

Davies, C. J. (2015). Cooling history of Earth's core with high thermal conductivity. *Physics of the Earth and Planetary Interiors*, *247*, 65–79. https://doi.org/10.1016/j.pepi.2015.03.007

Davies, C. J., & Pommier, A. (2018). Iron snow in the Martian core? *Earth and Planetary Science Letters*, *481*, 189–200. https://doi.org/10.1016/j.epsl.2017.10.026

Driscoll, P., & Davies, C. (2023). The "new core paradox": Challenges and potential solutions. *Journal of Geophysical Research: Solid Earth*, *128*(1), e2022JB025355. https://doi.org/10.1029/2022jb025355

Edmund, E., Morard, G., Baron, M. A., Rivoldini, A., Yokoo, S., Boccato, S., et al. (2022). The Fe-FeSi phase diagram at Mercury's core conditions. *Nature Communications*, *13*(1), 387. https://doi.org/10.1038/s41467-022-27991-9

Ezenwa, I. C., & Fei, Y. (2023). High pressure melting curve of Fe determined by inter-metallic fast diffusion technique. *Geophysical Research Letters*, *50*(6), e2022GL102006. https://doi.org/10.1029/2022gl102006

Ezenwa, I. C., Fei, Y., Hrubiak, R., & Kenney-Benson, C. (2024). High pressure melting curve of Fe-Si: Implication for the thermal properties in Mercury's core [Dataset]. *Open Science Framework*. https://doi.org/10.17605/OSF.IO/MGQT9

Ezenwa, I. C., & Secco, R. A. (2019). Fe melting transition: Electrical resistivity, thermal conductivity, and heat flow at the inner core boundaries of mercury and Ganymede. *Crystals*, *9*(7), 359. https://doi.org/10.3390/cryst9070359

Ezenwa, I. C., & Yoshino, T. (2020). Electrical resistivity of solid and liquid Pt: Insight into electrical resistivity of ε-Fe. *Earth and Planetary Science Letters*, *544*, 116380. https://doi.org/10.1016/j.epsl.2020.116380

Ezenwa, I. C., & Yoshino, T. (2021). Martian core heat flux: Electrical resistivity and thermal conductivity of liquid Fe at Martian core PT conditions. *Icarus*, *360*, 114367. https://doi.org/10.1016/j.icarus.2021.114367

Fei, Y., & Bertka, C. (2005). The interior of Mars. *Science*, *308*(5725), 1120–1121. https://doi.org/10.1126/science.1110531
Fischer, R. A., Campbell, A. J., Caracas, R., Reaman, D. M., Dera, P., & Prakapenka, V. B. (2012). Equation of state and phase diagram of Fe–16Si alloy as a candidate component of Earth's core. *Earth and Planetary Science Letters*, *357*, 268–276. https://doi.org/10.1016/j.epsl.2012.09.022
Fischer, R. A., Campbell, A. J., Reaman, D. M., Miller, N. A., Heinz, D. L., Dera, P., & Prakapenka, V. B. (2013). Phase relations in the Fe–FeSi system at high pressures and temperatures. *Earth and Planetary Science Letters*, *373*, 54–64. https://doi.org/10.1016/j.epsl.2013.04.035
Gessmann, C. K., Wood, B. J., Rubie, D. C., & Kilburn, M. R. (2001). Solubility of silicon in liquid metal at high pressure: Implications for the composition of the Earth's core. *Earth and Planetary Science Letters*, *184*(2), 367–376. https://doi.org/10.1016/s0012-821x(00)00325-3
Grott, M., Breuer, D., & Laneuville, M. (2011). Thermo-chemical evolution and global contraction of Mercury. *Earth and Planetary Science Letters*, *307*(1–2), 135–146. https://doi.org/10.1016/j.epsl.2011.04.040
Hauck, S. A., Margot, J. L., Solomon, S. C., Phillips, R. J., Johnson, C. L., Lemoine, F. G., et al. (2013). The curious case of Mercury's internal structure. *Journal of Geophysical Research: Planets*, *118*(6), 1204–1220. https://doi.org/10.1002/jgre.20091
Hauck II, S. A., Dombard, A. J., Phillips, R. J., & Solomon, S. C. (2004). Internal and tectonic evolution of Mercury. *Earth and Planetary Science Letters*, *222*(3–4), 713–728. https://doi.org/10.1016/j.epsl.2004.03.037
Hemingway, D. J., & Driscoll, P. E. (2021). History and future of the Martian dynamo and implications of a hypothetical solid inner core. *Journal of Geophysical Research: Planets*, *126*(4), e2020JE006663. https://doi.org/10.1029/2020je006663
Hirose, K., & Fei, Y. (2002). Subsolidus and melting phase relations of basaltic composition in the upper most lower mantle. *Geochimica et Cosmochimica Acta*, *66*(12), 2099–2108. https://doi.org/10.1016/s0016-7037(02)00847-5
Jamieson, J. C., & Lawson, A. W. (1962). X-ray diffraction studies in the 100 kilo bar pressure range. *Journal of Applied Physics*, *33*(3), 776–780. https://doi.org/10.1063/1.1777167
Khan, A., Liebske, C., Antoine, R., Attilio, R., Francis Nimmo, J. A. D., & Connolly, A.-C. (2018). Plesa, and Domenico Giardini. "A geophysical perspective on the bulk composition of Mars. *Journal of Geophysical Research: Planets*, *123*, 575–611. https://doi.org/10.1002/2017JE005371
Knibbe, J. S., & van Westrenen, W. (2018). The thermal evolution of Mercury's Fe–Si core. *Earth and Planetary Science Letters*, *482*, 147–159. https://doi.org/10.1016/j.epsl.2017.11.006
Kono, Y., Irifune, T., Higo, Y., Inoue, T., & Barnhoorn, A. (2010). PVT relation of MgO derived by simultaneous elastic wave velocity and in situ X-ray measurements: A new pressure scale for the mantle transition region. *Physics of the Earth and Planetary Interiors*, *183*(1–2), 196–211. https://doi.org/10.1016/j.pepi.2010.03.010
Kono, Y., Kenney-Benson, C., Shibazaki, Y., Park, C., Shen, G., & Wang, Y. (2015). High-pressure viscosity of liquid Fe and FeS revisited by falling sphere viscometry using ultrafast X-ray imaging. *Physics of the Earth and Planetary Interiors*, *241*, 57–64. https://doi.org/10.1016/j.pepi.2015.02.006
Kono, Y., Park, C., Kenney-Benson, C., Shen, G., & Wang, Y. (2014). Toward comprehensive studies of liquids at high pressures and high temperatures: Combined structure, elastic wave velocity, and viscosity measurements in the Paris–Edinburgh cell. *Physics of the Earth and Planetary Interiors*, *228*, 269–280. https://doi.org/10.1016/j.pepi.2013.09.006
Kubaschewski, O. (1982). *Iron-binary phase diagrams*. ISBN 978-3-662-08024-5 (pp. 136–137). Springer-Verlag, Verlag Stahleisen.
Kuwayama, Y., & Hirose, K. (2004). Phase relations in the system Fe-FeSi at 21 GPa. *American Mineralogist*, *89*(2–3), 273–276. https://doi.org/10.2138/am-2004-2-303
Lennard-Jones, J. E., & Devonshire, A. F. (1939). Critical and co-operative phenomena. IV. A theory of disorder in solids and liquids and the process of melting. *Proceedings of the Royal Society of London - Series A: Mathematical and Physical Sciences*, *170*(943), 464–484.
Lin, J. F., Heinz, D. L., Campbell, A. J., Devine, J. M., & Shen, G. (2002). Iron-silicon alloy in Earth's core? *Science*, *295*(5553), 313–315. https://doi.org/10.1126/science.1066932
Loper, D. E. (1978). Some thermal consequences of a gravitationally powered dynamo. *Journal of Geophysical Research*, *83*(B12), 5961–5970. https://doi.org/10.1029/jb083ib12p05961
Mao, H. K., Bassett, W. A., & Takahashi, T. (1967). Effect of pressure on crystal structure and lattice parameters of iron up to 300 kbar. *Journal of Applied Physics*, *38*(1), 272–276. https://doi.org/10.1063/1.1708965
Marchi, S., Chapman, C. R., Fassett, C. I., Head, J. W., Bottke, W. F., & Strom, R. G. (2013). Global resurfacing of Mercury 4.0–4.1 billion years ago by heavy bombardment and volcanism. *Nature*, *499*(7456), 59–61. https://doi.org/10.1038/nature12280
Margot, J. L., Peale, S. J., Jurgens, R. F., Slade, M. A., & Holin, I. V. (2007). Large longitude liberation of Mercury reveals a molten core. *Science*, *316*(5825), 710–714. https://doi.org/10.1126/science.1140514
McCubbin, F. M., Vander Kaaden, K. E., Peplowski, P. N., Bell, A. S., Nittler, L. R., Boyce, J. W., et al. (2017). A low O/Si ratio on the surface of mercury: Evidence for silicon smelting? *Journal of Geophysical Research: Planets*, *122*(10), 2053–2076. https://doi.org/10.1002/2017je005367
Meco, H., & Napolitano, R. E. (2005). Liquidus and solidus boundaries in the vicinity of order–disorder transitions in the Fe–Si system. *Scripta Materialia*, *52*(3), 221–226. https://doi.org/10.1016/j.scriptamat.2004.09.026
Ohta, K., Kuwayama, Y., Hirose, K., Shimizu, K., & Ohishi, Y. (2016). Experimental determination of the electrical resistivity of iron at Earth's core conditions. *Nature*, *534*(7605), 95–98. https://doi.org/10.1038/nature17957
Ozawa, H., Hirose, K., Yonemitsu, K., & Ohishi, Y. (2016). High-pressure melting experiments on Fe–Si alloys and implications for silicon as a light element in the core. *Earth and Planetary Science Letters*, *456*, 47–54. https://doi.org/10.1016/j.epsl.2016.08.042
Pommier, A., Driscoll, P. E., Fei, Y., & Walter, M. J. (2022). Investigating metallic cores using experiments on the physical properties of liquid iron alloys. *Frontiers in Earth Science*, *10*, 956971. https://doi.org/10.3389/feart.2022.956971
Rivoldini, A., & Van Hoolst, T. (2013). The interior structure of Mercury constrained by the low-degree gravity field and the rotation of Mercury. *Earth and Planetary Science Letters*, *377*, 62–72. https://doi.org/10.1016/j.epsl.2013.07.021
Rutter, M. D., Secco, R. A., Liu, H., Uchida, T., Rivers, M. L., Sutton, S. R., & Wang, Y. (2002). Viscosity of liquid Fe at high pressure. *Physical Review B*, *66*(6), 060102. https://doi.org/10.1103/physrevb.66.060102
Sanloup, C., Guyot, F., Gillet, P., & Fei, Y. (2002). Physical properties of liquid Fe alloys at high pressure and their bearings on the nature of metallic planetary cores. *Journal of Geophysical Research*, *107*(B11), ECV–4. https://doi.org/10.1029/2001jb000808
Sanloup, C., Guyot, F., Gillet, P., Fiquet, G., Hemley, R. J., Mezouar, M., & Martinez, I. (2000). Structural changes in liquid Fe at high pressures and high temperatures from synchrotron X-ray diffraction. *Europhysics Letters*, *52*(2), 151–157. https://doi.org/10.1209/epl/i2000-00417-3
Schurmann, E., & Hensgen, U. (1980). Studies of the melting equilibria in the system iron--silicon. *Arch. Eisenhuttenwes.*, *51*(1), 1–4. https://doi.org/10.1002/srin.198004792
Secco, R. A. (2017). Thermal conductivity and Seebeck coefficient of Fe and Fe-Si alloys: Implications for variable Lorenz number. *Physics of the Earth and Planetary Interiors*, *265*, 23–34. https://doi.org/10.1016/j.pepi.2017.01.005

Silber, R. E., Secco, R. A., Yong, W., & Littleton, J. A. (2019). Heat flow in Earth's core from invariant electrical resistivity of Fe-Si on the melting boundary to 9 GPa: Do light elements matter? *Journal of Geophysical Research: Solid Earth*, *124*(6), 5521–5543. https://doi.org/10.1029/2019jb017375

Steinbrügge, G., Dumberry, M., Rivoldini, A., Schubert, G., Cao, H., Schroeder, D. M., & Soderlund, K. M. (2021). Challenges on Mercury's interior structure posed by the new measurements of its obliquity and tides. *Geophysical Research Letters*, *48*(3), e2020GL089895. https://doi.org/10.1029/2020gl089895

Tao, R., & Fei, Y. (2021). High-pressure experimental constraints of partitioning behavior of Si and S at the Mercury's inner core boundary. *Earth and Planetary Science Letters*, *562*, 116849. https://doi.org/10.1016/j.epsl.2021.116849

Tateyama, R., Ohtani, E., Terasaki, H., Nishida, K., Shibazaki, Y., Suzuki, A., & Kikegawa, T. (2011). Density measurements of liquid Fe–Si alloys at high pressure using the sink–float method. *Physics and Chemistry of Minerals*, *38*(10), 801–807. https://doi.org/10.1007/s00269-011-0452-1

Terasaki, H., Kato, T., Urakawa, S., Funakoshi, K., Sato, K., Suzuki, A., & Okada, T. (2002). Viscosity change and structural transition of molten Fe at 5 GPa. *Geophysical Research Letters*, *29*(8), 68–71. https://doi.org/10.1029/2001gl014321

Terasaki, H., Rivoldini, A., Shimoyama, Y., Nishida, K., Urakawa, S., Maki, M., et al. (2019). Pressure and composition effects on sound velocity and density of core-forming liquids: Implication to core compositions of terrestrial planets. *Journal of Geophysical Research: Planets*, *124*(8), 2272–2293. https://doi.org/10.1029/2019je005936

Tosi, N., Grott, M., Plesa, A. C., & Breuer, D. (2013). Thermochemical evolution of Mercury's interior. *Journal of Geophysical Research: Planets*, *118*(12), 2474–2487. https://doi.org/10.1002/jgre.20168

Weber, R. C., Lin, P. Y., Garnero, E. J., Williams, Q., & Lognonné, P. (2011). Seismic detection of the lunar core. *Science*, *331*(6015), 309–312. https://doi.org/10.1126/science.1199375

Yamazaki, D., Ito, E., Yoshino, T., Yoneda, A., Guo, X., Zhang, B., et al. (2012). P-V-T equation of state for ε-iron up to 80 GPa and 1900 K using the Kawai-type high pressure apparatus equipped with sintered diamond anvils. *Geophysical Research Letters*, *39*(20). https://doi.org/10.1029/2012gl053540

Yang, H., & Secco, R. A. (1999). Melting boundary of Fe-17% Si up to 5.5 GPa and the timing of core formation. *Geophysical Research Letters*, *26*(2), 263–266. https://doi.org/10.1029/1998gl900292

Yin, Y., Wang, L., Zhai, S., & Fei, Y. (2022). Electrical resistivity of Fe and Fe-3 wt% P at 5 GPa with implications for the Moon's core conductivity and dynamo. *Journal of Geophysical Research: Planets*, *127*(4), e2021JE007116. https://doi.org/10.1029/2021je007116

Yu, X., & Secco, R. A. (2008). Equation of state of liquid Fe–17 wt% Si to 12 GPa. *High Pressure Research*, *28*(1), 19–28. https://doi.org/10.1080/08957950701882138

Zhang, J., & Guyot, F. (1999). Experimental study of the bcc-fcc phase transformations in the Fe-rich system Fe-Si at high pressures. *Physics and Chemistry of Minerals*, *26*(6), 419–424. https://doi.org/10.1007/s002690050203

Zhang, Y., Hou, M., Liu, G., Zhang, C., Prakapenka, V. B., Greenberg, E., et al. (2020). Reconciliation of experiments and theory on transport properties of iron and the geodynamo. *Physical Review Letters*, *125*(7), 078501. https://doi.org/10.1103/physrevlett.125.078501

Zolotov, M. Y., Sprague, A. L., Hauck, S. A., Nittler, L. R., Solomon, S. C., & Weider, S. Z. (2013). The redox state, FeO content, and origin of sulfur-rich magmas on Mercury. *Journal of Geophysical Research: Planets*, *118*(1), 138–146. https://doi.org/10.1029/2012je004274